Immuno-PET Imaging of Tumor Endothelial Marker 8 (TEM8)

Frank Kuo,[†,‡] Stephanie Histed,[†,‡] Biying Xu,[§] Veerendra Bhadrasetty,[†] Lawrence P. Szajek,[∥] Mark R. Williams,[†] Karen Wong,[†] Haitao Wu,[§] Kelly Lane,[§] Vincent Coble,[§] Olga Vasalatiy,[§] Gary L. Griffiths,[⊥] Chang H. Paik,[#] Osama Elbuluk,[†] Christopher Szot,[¶] Amit Chaudhary,[¶] Brad St. Croix,[¶] Peter Choyke,[†] and Elaine M. Jagoda*,[†]

[†]Molecular Imaging Program, National Cancer Institute, Bethesda, Maryland 20892-1088, United States

[§]Imaging Probe Development Center, National Heart, Lung, and Blood Institute, National Institutes of Health, Rockville, Maryland 20892-3372, United States

[∥]PET Department and [#]Nuclear Medicine Division, Radiology and Imaging Sciences, Clinical Center, National Institutes of Health, Bethesda, Maryland 20892, United States

[⊥]Clinical Research Directorate/CMRP, Leidos Biomedical Research Inc. (formerly SAIC-Frederick, Inc.), Frederick National Laboratory for Cancer Research, Frederick, Maryland 21702, United States

[¶]Tumor Angiogenesis Section, Mouse Cancer Genetics Program, National Cancer Institute, Frederick, Maryland 21702, United States

ABSTRACT: Tumor endothelial marker 8 (TEM8) is a cell surface receptor that is highly expressed in a variety of human tumors and promotes tumor angiogenesis and cell growth. Antibodies targeting TEM8 block tumor angiogenesis in a manner distinct from the VEGF receptor pathway. Development of a TEM8 imaging agent could aid in patient selection for specific antiangiogenic therapies and for response monitoring. In these studies, L2, a therapeutic anti-TEM8 monoclonal IgG antibody (L2mAb), was labeled with ^{89}Zr and evaluated in vitro and in vivo in TEM8 expressing cells and mouse xenografts (NCI-H460, DLD-1) as a potential TEM8 immuno-PET imaging agent. ^{89}Zr-df–L2mAb was synthesized using a desferrioxamine–L2mAb conjugate (df–L2mAb); ^{125}I-L2mAb was labeled directly. In vitro binding studies were performed using human derived cell lines with high, moderate, and low/undetectable TEM8 expression. ^{89}Zr-df–L2mAb in vitro autoradiography studies and CD31 IHC staining were performed with cryosections from human tumor xenografts (NCI-H460, DLD-1, MKN-45, U87-MG, T-47D, and A-431). Confirmatory TEM8 Western blots were performed with the same tumor types and cells. ^{89}Zr-df–L2mAb biodistribution and PET imaging studies were performed in NCI-H460 and DLD-1 xenografts in nude mice. ^{125}I-L2mAb and ^{89}Zr-df–L2mAb exhibited specific and high affinity binding to TEM8 that was consistent with TEM8 expression levels. In NCI-H460 and DLD-1 mouse xenografts nontarget tissue uptake of ^{89}Zr-df–L2mAb was similar; the liver and spleen exhibited the highest uptake at all time points. ^{89}Zr-L2mAb was highly retained in NCI-H460 tumors with <10% losses from day 1 to day 3 with the highest tumor to muscle ratios (T:M) occurring at day 3. DLD-1 tumors exhibited similar pharmacokinetics, but tumor uptake and T:M ratios were reduced ~2-fold in comparison to NCI-H460 at all time points. NCI-H460 and DLD-1 tumors were easily visualized in PET imaging studies despite low in vitro TEM8 expression in DLD-1 cells indicating that in vivo expression might be higher in DLD-1 tumors. From in vitro autoradiography studies ^{89}Zr-df–L2mAb specific binding was found in 6 tumor types (U87-MG, NCI-H460, T-47D MKN-45, A-431, and DLD-1) which highly correlated to vessel density (CD31 IHC). Westerns blots confirmed the presence of TEM8 in the 6 tumor types but found undetectable TEM8 levels in DLD-1 and MKN-45 cells. This data would indicate that TEM8 is associated with the tumor vasculature rather than the tumor tissue, thus explaining the increased TEM8 expression in DLD-1 tumors compared to DLD-1 cell cultures. ^{89}Zr-df–L2mAb specifically targeted TEM8 in vitro and in vivo although the in vitro expression was not necessarily predictive of in vivo expression which seemed to be associated with the tumor vasculature. In mouse models, ^{89}Zr-df–L2mAb tumor uptakes and T:M ratios were sufficient for visualization during PET imaging. These results would suggest that a TEM8 targeted PET imaging agent, such as ^{89}Zr-df–L2mAb, may have potential clinical, diagnostic, and prognostic applications by providing a quantitative measure of tumor angiogenesis and patient selection for future TEM8 directed therapies.

KEYWORDS: immuno-PET imaging, TEM8, anti-TEM8 antibodies, L2, [^{89}Zr]-df–L2mAb, angiogenesis
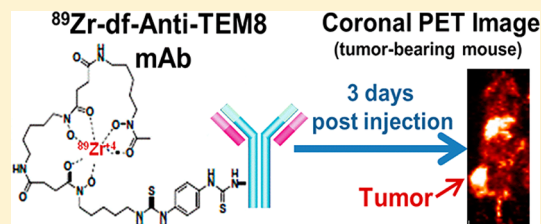
INTRODUCTION

Angiogenesis is critical to sustain and promote tumor growth, and numerous antiangiogenic drugs are in clinical use. Many of these agents are directed toward the VEGF pathway utilizing blocking antibodies (bevacizumab) and/or VEGFR receptor tyrosine kinase inhibitors among others. Recently another promising antiangiogenic therapeutic target, tumor endothelial cell marker 8 (TEM8), has been identified to which blocking antibodies are currently under development.[1,2] Positron emission tomography (PET) imaging agents designed to detect these tumor angiogenenic targets could aid in drug development as well as improve patient outcomes by correctly selecting patients for therapy as well as accurately assessing efficacy. In this regard, changes in tumor size are insensitive and can typically lag months behind the actual tumor response.[3] PET imaging, however, has the advantage of providing early measurement of responses using the same molecular target as the therapeutic agent.

Vascular endothelial growth factors (VEGF), VEGF receptors (VEGFRs) integrins $(\alpha_v\beta_3)$, and matrix metalloproteinases (MMPs) have all been identified as targets of angiogenesis to which imaging and therapeutic agents can be directed.[4] Several targeted imaging agents have been described that make use of radiolabeled VEGF or monoclonal antibodies against VEGF, such as HuMV833, VG76e, or bevacizumab.[5−8] $[^{18}F]$-Flucicla-tide, a small radiolabeled cyclic peptide containing the RGD tripeptide which binds with high affinity to $\alpha_v\beta_3$ integrins, has also shown promise in imaging angiogenesis.[9] In both preclinical and clinical studies, reductions in $[^{18}F]$-fluciclatide uptake were associated with decreased $\alpha_v\beta_3$ integrin expression and an early response to antiangiogenic targeted therapy.[10−12] In other preclinical studies targeting MMPs, ^{18}F-labeled marimastat, an MMP inhibitor, and MMP2/9 substrate were shown to localize to tumors.[13−15] Thus, radiolabeling of therapeutic antiangiogenic agents is firmly established in the literature.

In addition to the angiogenic markers described above, at least 46 targets with therapeutic potential have been identified on endothelial cells of tumor vasculature. These tumor endothelial markers, also known as TEMs, represent a group of genes involved in the process of angiogenesis.[16] One of these, TEM8, has been found to be upregulated on tumor vessels in several tumor types in both humans and tumor-bearing mouse models but not in normal reparative angiogenesis associated with wound healing or ovulation.[16−20] TEM8 is a type I transmembrane protein (564 amino acids in length) with an extracellular domain similar to αD integrin that interacts with endothelial adhesion molecules. Endothelial cell adhesion, migration, and tubule formation are promoted by TEM8, suggesting a role in angiogenesis.[2,21] Interestingly, TEM8 has also been identified as the anthrax toxin receptor (ANTXR1)[22,23] and shares the extracellular von Willebrand factor type A (vWA) domain with another anthrax toxin receptor known as capillary morphogenesis protein 2 (CMG2/ANTXR2).[16,22,23] Studies have shown that inhibiting TEM8 activity with TEM8 vaccines or TEM8-Fc antibody-like molecules slowed tumor growth in tumor-bearing mouse models; similarly in tumor-bearing TEM8 knockout mice, tumor growth was impaired compared to wild types.[24−29] Hence targeting TEM8 may have both diagnostic potential and therapeutic value. Although a 13 amino acid peptide targeting TEM8 was successfully radiolabeled with ^{18}F, in preclinical studies this PET imaging agent exhibited low affinity binding to TEM8 and low retention in vivo in TEM8 + human tumors in xenograft mice.[30]

Several therapeutic monoclonal antibodies against TEM8 are under development which may provide suitable platforms for PET imaging agents.[25] One of these, L2mAb, is an anti-TEM8 human-mouse reverse chimeric monoclonal antibody (human variable regions and murine constant domains) which has a high affinity and specificity for the vWA domain of TEM8 and has been found to localize to tumor vasculature.[16,25] In tumor challenge studies, either treatment of mice with L2mAb or genetic disruption in the host (tumor-bearing TEM8 knockout mice) resulted in delayed growth of colorectal adenocarcinoma (DLD-1), non-small cell lung carcinoma (NCI-H460), and melanoma (UACC) human xenograft tumors.[24] However, neither pharmacological nor genetic ablation of TEM8 had any discernible effect on normal physiologic angiogenesis. The reduced tumor-igenicity in the TEM8 knockout suggests that TEM8 functions to promote tumor angiogenesis. Anti-TEM8 antibodies may block this pro-angiogenic function and/or elicit natural killer cell mediated and complement-mediated cytotoxicity.[16,24,25]

Thus, the selectivity of L2mAb for tumor vasculature and its high affinity for TEM8 would suggest that L2mAb may be suitable for imaging both as a diagnostic tool and as a means to monitor therapy.[31] Therefore, we initially evaluated ^{125}I-L2mAb to assess in vitro binding characteristics of L2mAb and L2mAb after conjugation to the bifunctional chelate, desferrioxamine (df−L2mAb), required for the radiolabeling with ^{89}Zr. Desferrioxamine is a strong chelator for ^{89}Zr with suitable in vivo stability, and efficient radiolabeling methods for mAbs have been developed.[32,33] After these preliminary studies, ^{89}Zr ($T_{1/2}$ = 3.3 days) was chelated to df−L2mAb (^{89}Zr-df−L2mAb), and affinity (K_d), biological activity (% immunoreactivity), and TEM8 concentrations were determined using human cell lines with a known range of TEM8 expression. From in vitro auto-radiography studies TEM8 concentrations were assessed in various tumor types and then correlated with vessel density (CD31 IHC staining) and TEM8 immunoprecipitation Western blots (IP Westerns). Finally, in vivo biodistribution and PET imaging studies were performed to determine the localization of ^{89}Zr-df−L2mAb in tumor-bearing mice.

EXPERIMENTAL SECTION

Cell Lines and Reagents. Cell lines were grown at 37 °C in 5% CO_2 in RPMI-1640, 0.1 mM NEAA, and 1 mM sodium pyruvate [NCI-H460 (NSCLC), DLD-1 (colorectal adenocarci-noma), MKN-45 (gastric carcinoma), T-47D (breast ductal carcinoma), A-431 (epidermoid carcinoma) cells], or DMEM, 0.1 mM NEAA, and 1 mM sodium pyruvate [U87-MG (glioblastoma astrocytoma), HEK-293 (parental human embryonic kidney), HEK-293 flag (HEK-293 +F, HEK-293 transfected with flag-tagged human TEM-8) cells].[25] All media were supplemented with 10% FBS, 2 mM L-glutamine, and Pen/Strep/Amphotericin B.

Anti-TEM8 antibody (L2mAb, human-mouse chimeric mAb with human variable domains and murine IgG2a constant domains) was provided by Dr. Brad St. Croix (NCI-Frederick, Frederick, MD).[25]

Desferrioxamine−L2mAb Conjugate Procedure and Characterization. L2mAb was conjugated to desferrioxamine (df) through an isothiocyanate linker, p-isothiocyanatobenzyl-desferrioxamine (Macrocyclics, Inc., Dallas, TX), to produce desferrioxamine−L2mAb (df−L2mAb) conjugates by reacting the df with L2mAb in molar ratios (df:L2mAb) of 3:1 (R3), 5:1 (R5), 10:1 (R10), and 12:1 (R12) using a conjugation procedure previously described.[33,34]

The number of chelates per L2mAb antibody was determined using a titration assay reported by Meares et al.[35] Briefly, conjugate aliquots were allowed to react with 10-fold excess of 25 mM zirconium chloride trace mixed with carrier free ^{89}Zr (37 MBq; 1.0 mCi) oxalate according to the published radiolabeling protocol.[36] Unmodified L2mAb antibody was used as a control. For the R10 conjugate the number of chelates conjugated per L2mAb was 2.5 ± 0.1, which was incorporated into the calculation of the final specific activity.

Radiosynthesis of ^{89}Zr-df−anti-TEM8 Ab (^{89}Zr-df−L2mAb) and ^{125}I-anti-TEM8 Ab (^{125}I-L2mAb). The radio-synthesis of ^{89}Zr-df−L2mAb was accomplished using a modified method of Perk et al.[33] Briefly, purified ^{89}Zr(IV) [37−74 MBq; 1−2 mCi] in 1 M oxalic acid was neutralized with Na$_2$CO$_3$ (2 M) and HEPES (0.5 M, pH = 7.0) and reacted with the df−L2mAb R10 conjugate [700 μg (7 mg/mL), 0.25 M sodium acetate buffer, pH 5.5] in ascorbic or gentisic acid (5 mg/mL) and/or 1% BSA to yield ^{89}Zr-df−L2mAb. The labeled products were purified with a size exclusion PD-10 column eluted with 0.25 M sodium acetate, pH 5.3, or PBS, pH 6.8. Typical radiochemical labeling yields determined by size exclusion HPLC with UV monitoring were >90%, with specific activities at the end of synthesis (EOS) ranging from 0.074 to 0.222 MBq/μg. To assess the stability of these ^{89}Zr-df−L2mAb batches, the reaction mixtures were stored at 4 °C and analyzed by size exclusion HPLC 0, 24, and 48 h after radiosynthesis. The ^{89}Zr-oxalate preparations used in the biodistribution studies were neutralized as described above.

The radiosynthesis of ^{125}I-L2mAb was accomplished following the Pierce Pre-Coated Iodination Tubes indirect iodination method. Briefly, a Pierce Pre-Coated Iodo-Gen Iodination Tube was wetted with 1 mL of Tris Iodination Buffer (25 mM Tris·HCl, pH 7.5, 0.4 M NaCl) and then decanted, after which Tris Iodination Buffer (50 μL) and 74 MBq (2 mCi) Na^{125}I solution (PerkinElmer) was added. The activated iodide solution was transferred into a 1.5 mL eppendorf vial containing L2mAb protein solution (100 μL, 0.2 mg/mL) in PBS. The mixture was reacted, and then 50 μL of aqueous saturated tyrosine scavenging buffer was added. After mixing and incubating, the sample was added to a mini-PD10 pre-equilibrated with 8 mL of Tris/BSA buffer [0.25% bovine serum albumin (2.5 mg/mL), 25 mM Tris·HCl, pH 7.5, 0.4 M NaCl, 5 mM EDTA, 0.05% sodium azide]. The flow through was discarded, and the protein fraction was collected. Typical labeling yields determined by size exclusion HPLC with UV monitoring were >90%, with specific activities (EOS) ranging from 0.3478 to 0.7808 MBq/μg.

In Vitro Studies. Saturation binding studies were performed to determine the K_d and B_{max} using plated cells (NCI-H460 or DLD-1; 2−10 × 10^5 cells/well) or cells (nonadherent) in tubes (HEK-293 or HEK-293 F+; 2−10 × 10^5 cells/tube) to which increasing concentrations of radiolabeled L2mAb (0.15−52 nM) were added to duplicate tubes; nonspecific binding was determined by adding unlabeled L2mAb (10^{-6} M) to another set of duplicates. For competition studies, radio-labeled L2mAb at a single concentration (0.15 to 2.9 nM) and increasing concentrations (0−1000 nM) of competitors [L2mAb; df−L2mAb conjugates (R3, R5, R10, and R12)] were added to NCI-H460 or HEK-293 F+ cells. After incubation (2 h, 4 °C), the cell bound radiolabeled L2mAb was separated from free antibody: (1) plated cells were washed with phosphate buffered saline (PBS), treated with trypsin, and collected in vials; or (2) cells in tubes were pelleted by centrifugation and washed twice (PBS), and supernatants were removed. The cell bound

radioactivity for these samples was determined by gamma counting (PerkinElmer 2480 Wizard3, Shelton, CT). From the saturation studies the K_d and B_{max} were determined from at least 6 to 8 concentrations of radiolabeled L2mAb and analyzed using nonlinear regression curve fits (one-site specific binding); from the competition studies K_i's were determined from 8 competitor concentrations [PRISM (version 5.04 Windows), GraphPad software, San Diego, CA].

The biological specific activity or immunoreactive fraction (% immunoreactivity) of the radiolabeled L2mAbs was determined by a modified method previously described by Morris.[37] Briefly, the % immunoreactivity was determined by a self-displacement method derived from a radiolabeled L2mAb saturation curve and competition curve using, as the competitor, unlabeled L2mAb.

Mouse Tumor Models. Athymic female nude mice (Ncr-nu/nu, NCI-Frederick, MD) were injected subcutaneously in the right thigh with either NCI-H460, DLD-1, MKN-45, U87-MG, T-47D, or A-431 cells ((5−8) × 10^6) in PBS:30% matrigel. All animal studies were performed in accordance with NIH Guidelines for the Care and Use of Laboratory Animals using IACUC approved protocols.

Biodistribution Studies. Control or tumor-bearing mice (tumor weights: 0.2−3.7 g) were injected while awake via the tail vein with ^{89}Zr-df−L2mAb [0.37−0.74 MBq (10 to 20 μCi, 8 to 16 pmol] or ^{89}Zr-oxalate (neutralized) [0.185−0.74 MBq] and then were euthanized (via CO$_2$ inhalation) at selected times. Blood and tissues were excised from each animal and weighed, and radioactivity was determined (PerkinElmer 2480 Wizard3). Radioactivity in the blood and each tissue was expressed as % injected dose per gram of tissue (% ID/g) normalized to a 20 g mouse: 100[counts per minute (cpm)$_{tissue}$]/[cpm$_{injected\ dose}$ × tissue weight (g)] × (body weight/20). Correlation between % ID/tumor and tumor weight was performed using linear regression analysis. Statistical analysis between the 2 groups was performed with the Student t test.

In Vitro Autoradiography and Histological Staining. NCI-H460, DLD-1, MKN-45, U87-MG, T-47D, and A-431 cell xenograft tumors were excised, rapidly frozen in dry ice, and stored until use. The tumors were sectioned into 20 μm slices (Leica CM3050S) and allowed to air-dry before use. Mounted slides were preincubated in the incubation buffer [TRIS 50 mM (pH 7.5), 10 nM MgCl$_2$, 2 mM EGTA, 0.1% BSA, 0.15 mM bacitracin, 100 KI units/mL aprotinin] for 15 min at room temperature, and then incubated for 2 h in baths of ^{89}Zr-df−L2mAb (10 to16 nM) or ^{89}Zr-df−L2mAb (10 to 16 nM) + L2mAb (700 nM). After incubation the slides were rinsed twice (50 mM TRIS, 4 °C) for 2 min, dipped in distilled water, allowed to dry, and exposed to phosphorimaging plates (Fuji BAS-SR2025).

Following exposure for 48 to 72 h, the plates were scanned with the Fuji FLA-5100 scanner to produce digitized images. Regions of interest (ROIs) from the digitized images, expressed as photostimulated luminescence units per mm^2 (PSL/mm^2), were drawn for the whole tumor slice, and the high and low density areas within the section, using Image Gauge 4.0 (Fujifilm, Tokyo, Japan) which represented ^{89}Zr-df−L2mAb "total" binding (B_t). To determine the nonspecific binding (B_{nsb}) similar ROIs in adjacent sections from the "+ 700 nM" L2mAb bath were also measured. The ROIs representing specific ^{89}Zr-df−L2mAb binding (B_{sp}) were determined by subtracting B_{nsb} ROIs from B_t ROIs ($B_t − B_{nsb} = B_{sp}$). The TEM8 concentrations (nM) were determined by correlating the ROI units (PSL) to cpm which could be converted to molar concentrations

using the specific activity of ^{89}Zr-df—L2mAb as previously described.[38] Briefly, slides (6 to 8) after drying were counted on a PerkinElmer 2480 Wizard3 to determine the radioactive content (cpm) and then exposed to the phosphorimaging plate from which PSLs were determined by drawing an ROI encompassing the entire slide; using the PSL units and cpms associated with the slide, the linear relationship between PSLs and cpms (slope of the line) was determined for each study. Using this linear relationship (cpm = slope × PSL), ROIs could be converted from PSL/m^2 to cpm/m^2 and used to calculate the "relative" TEM8 molar concentrations (M_{rel}) in the tumor types which would be dependent on ^{89}Zr-df—L2mAb concentrations during the assay incubation time and the efficiency of collecting positron decay from a slice thickness of 20 μm.

For the CD31 PECAM-1 staining, tumor sections after air drying were fixed in acetone and, following an endogenous biotin block, were incubated in normal rabbit serum, followed by CD31 for 30 min (BD Bioscience #550274, diluted 1:100). Slides were rinsed, and then biotinylated rabbit a/rat IgG, mouse adsorbed (1:500; Vector Laboratories), was applied for 30 min. Endogenous peroxidase activity was assessed, followed by incubation in ABC reagent. The reaction was visualized with DAB, followed by hematoxylin counterstain. Slides were digitally scanned and quantitated for vessel density (Aperio, Leica Biosystems, Buffalo Grove, IL). The correlation of the CD31 IHC vessel counts to the tumor section ROIs were performed using the Spearman rank correlation coefficient [PRISM (version 5.04 Windows), GraphPad software, San Diego, CA].

Immunoprecipitation and Western Blotting. Tumors were homogenized with a lysing kit (Peqlab, Wilmington, DE), and total cell and tumor lysates were normalized with a BCA protein assay (Pierce). Lysates were immunoprecipitated overnight with a rabbit monoclonal anti-TEM8 antibody (produced as part of a collaboration between Epitomics and the National Cancer Institute). After immunoprecipitation using protein A agarose (Roche), protein extracts were separated by SDS—PAGE, transferred to a PDVF membrane (Millipore), and detected by immunoblotting with the rabbit monoclonal anti-TEM8 antibody followed by an HRP-conjugated anti-rabbit IgG, light chain specific secondary antibody (Jackson). Chemiluminescence was visualized with the ECL 2 Western blotting substrate (Pierce) according to the supplier's instructions.

MicroPet Imaging Studies. Tumor-bearing mice were anesthetized with isoflurane/O$_2$ (1.5%—3% v/v) and imaged at various times after intravenous injection of ^{89}Zr-df—L2mAb [~3.7 MBq, ~100 μCi, ~80 pmol]. Whole body static images were obtained at 4—5 bed positions (FOV = 2.0 cm, total imaging time: 20—25 min) using the Advanced Technology Laboratory Animal Scanner.[39] The images were reconstructed by a two-dimensional ordered-subsets expectation maximum (OSEM) from which regions of interest (ROIs) were drawn manually to determine the tissue uptakes (kBq/cc). The % ID/g normalized to a 20 g mouse was then determined using the formula (100 × tissue uptake/injected dose) × (body weight/20).

■ RESULTS

In Vitro Cell Binding Studies. Initial binding studies were performed with ^{125}I-L2mAb to determine its affinity (K_d) for TEM8, TEM8 concentrations in various cell lines (B_{max}, receptors per cell), % immunoreactive fraction (biological specific activity) of ^{125}I-L2mAb, and inhibition constants (K_i's) of desferrioxamine L2mAb conjugates (df—L2mAb) to determine the most optimal df:L2mAb conjugation ratio for

preparation of Zr^{89}-df—L2mAb. ^{125}I-L2mAb exhibited high TEM8 specific binding (74%—96%) and affinity for TEM8 with a K_d of 5.76 ± 1.59 nM ($n = 4$) in HEK-293 F+ (high TEM8 expression; transfected with a flag tagged TEM8 vector) and NCI-H460 cells (moderate TEM8 expression); the ^{125}I-L2mAb immunoreactive fraction was high, ranging from 82% to 91%. The concentration of TEM8 was higher for the HEK-293 F+ cells [$B_{max} = (4.44 ± 0.72) \times 10^5$ receptors per cell, $n = 2$] than the NCI-H460 cells [$B_{max} = (0.938 ± 0.174) \times 10^5$ receptors per cell, $n = 2$] as expected. In similar studies with DLD-1 cells, TEM8 concentrations [$B_{max} \leq (0.0517 ± 0.033) \times 10^5$ receptors per cell, $n = 2$ ($K_d = 5.76$ nM, as determined for ^{125}I-L2mAb)] were at least 10-fold lower than NCI-H460 cells with the majority of the bound ^{125}I-L2mAb representing nonspecific binding (69—98%). In the case of the parental cell line HEK-293 high nonspecific binding was observed (82—92%) and specific TEM8 binding could not be discerned ($n = 2$). In the competition assays with ^{125}I-L2mAb the K_i's of unlabeled L2mAb and df—L2mAb conjugates at molar ratios (df:L2mAb) of 3:1 (R3), 5:1 (R5), 10:1 (R10), and 12:1 (R12) were determined (Figure 1A). The L2mAb ($K_i = 2.68 ± 1.27$ nM; $n = 3$) had the highest K_i compared to the conjugates R3 ($K_i = 3.88$ nM), R5 ($K_i = 4.01$ nM), R10 ($K_i = 6.09$ nM), and R12 ($K_i = 9.16$ nM) in which the conjugate K_i's correspondingly increased with increasing molar ratios. These results indicated that the R10 conjugate represented the most appropriate balance between retention of high binding affinity for TEM8 and specific activity when labeled with ^{89}Zr.

^{89}Zr-df—L2mAb synthesized using the R(10) df—L2mAb conjugate had high TEM8 specific binding (61% to 99%) and affinity, $K_d = 1.85 ± 0.33$ nM ($n = 4$, ^{89}Zr-df—L2mAb batches) as determined from saturation binding studies in HEK-293 F+ and NCI-H460 cells (Figure 1B; representative HEK-293 F+ saturation binding curve). For these ^{89}Zr-df—L2mAb batches, the immunoreactive fraction was high, ranging from 95% to 99% at approximately 8 to 24 h after synthesis, but after storage for 3 days at 4 °C modest decreases in the immunoreactive fraction (75% to 70%) and affinity ($K_d \sim 3$ nM) were observed. In other studies in which stability was assessed by HPLC, the product peak (monomer) was relatively stable with <2% decreases observed from the end of synthesis (0 time) to 1 and 2 days after. The rank order of TEM8 concentrations in these cell lines using ^{89}Zr-df—L2mAb was comparable to that using ^{125}I-L2mAb in which HEK-293 F+ cells had the highest TEM8 concentrations [$B_{max} = (3.68 ± 0.18) \times 10^5$ receptors per cell; $n = 3$] with NCI-H460 ~ 4-fold less [$B_{max} = (0.84 ± 0.24) \times 10^5$ receptors per cell; $n = 3$] (Figure 1C). Low to undetectable TEM8 concentrations were found in DLD-1 cells [$B_{max} \leq (0.056 ± 0.0098) \times 10^5$ receptors per cell; $n = 2$ ($K_d = 1.54$ nM as determined for ^{89}Zr-df—L2mAb)], and high nonspecific binding (75% to 100%) was seen; no specific TEM8 binding in the parental HEK-293 cell line was detected ($n = 2$). These in vitro results indicate that ^{89}Zr-df—L2mAb would be appropriate for in vivo imaging of tumors with high to moderate TEM8 expression (>80,000 receptors per cell) as was observed with the HEK-293 F+ and NCI-H460 cells whereas tumors with low TEM8 expression (<6000 receptors per cell), as in the case of DLD-1, would not be detectable.

In Vivo ^{89}Zr-df—L2mAb and ^{89}Zr-Oxalate Biodistribution Studies. The biodistribution of ^{89}Zr-df—L2mAb was determined in NCI-H460 xenografts, during a period of 1 to 7 days postinjection (Figure 2A). The highest uptakes were observed in the nontarget tissues, spleen (45% to 27% ID/g) and liver (21% to 16% ID/g) at all times decreasing by 40% and 25%,
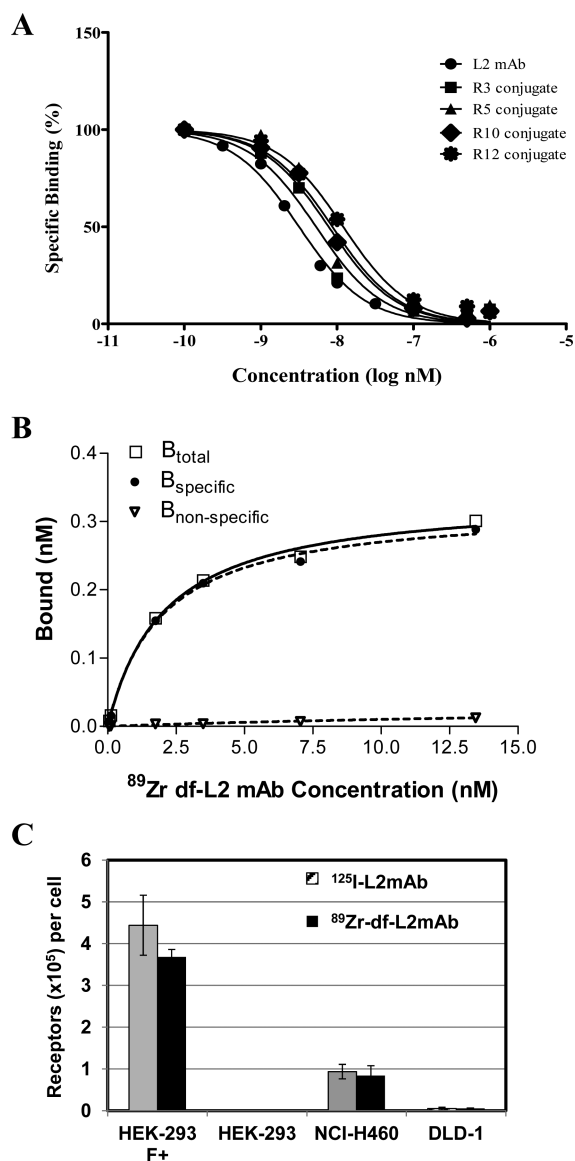
Figure 1. (A) In vitro ^{125}I-L2mAb competition-binding assay with NCI-H460 cells comparing L2mAb to df−L2mAb conjugates prepared at df to L2mAb ratios of 3:1 (R3), 5:1 (R5), 10:1 (R10), and 12:1 (R12). Each point (average of duplicates) represents % specific bound. (B) Representative in vitro [89]Zr-df−L2mAb saturation binding assay using HEK-293 F+ cells (transfected with TEM8) with each point representing the average of duplicates; K_d = 1.95 ± 0.22 (SE) nM; B_{max} = 0.32 ± 0.01 (SE) nM (3.88×10^5 receptors/cell); $B_{nonspecific}$ determined in the presence of 10^{-6} M L2mAb. (C) Comparison of TEM8 receptor concentrations for HEK-293 F+, HEK-293, NCI-H460, and DLD-1 determined from saturation binding assays with ^{125}I-L2mAb or [89]Zr-df−L2mAb. Each bar represents the mean ± SD (^{125}I-L2mAb, $n = 2$ for all cell lines; [89]Zr-df−L2mAb, $n = 3$ for HEK-293 F+ and NCI-H460, $n = 2$ for HEK-293 and DLD-1).

respectively, from day 1 to day 7. [89]Zr-df−L2mAb was highly retained in NCI-H460 tumors with <10% losses from day 1 (5.2% ID/g) to day 3 (4.7% ID/g) whereas clearance of [89]Zr-df−L2mAb from blood, muscle, heart, lungs, gastrointestinal tract, and kidney was faster with decreases in uptake (% ID/g) ranging from 34% to 62% over the same time (Figure 2B). This high tumor retention of [89]Zr-df−L2mAb would indicate high affinity binding to TEM8 as well as in vivo stability over the 3 day time course. However, tumor uptake at day 5 (2.4% ID/g) and day 7

(1.4% ID/g) was substantially reduced from day 1, respectively (Figure 2B). Most likely this increased clearance of radioactivity represents metabolism and lack of stability in the chelate with the loss of [89]Zr. This is confirmed by the 2- to 3-fold increase in bone uptake observed at day 5 (11.2% ID/g) and day 7 (11.8% ID/g) compared to day 1 (4.8% ID/g) as [89]Zr is known to localize in the bone.[32] In biodistribution studies using DLD-1 xenografts, uptake in nontarget tissues was comparable to that in NCI-H460 xenografts but DLD-1 tumor uptake (Figure 2B) was significantly lower (~2-fold) at day 1, day 3, and day 5 (P < 0.05) compared to NCI-H460 tumor uptake. This lower in vivo uptake in DLD-1 tumors compared to NCI-H460 tumors corresponded to the rank order of TEM8 expression determined in vitro although the magnitude of the difference between the DLD-1 cells and NCI-H460 cells (10- to 20-fold) was much greater than between tumors. Furthermore, examining the tumor to muscle ratios (T:M) over the 7 day time course revealed that the NCI-H460 tumors had the highest T:M of 13.3:1 at day 3 which decreased by >60% at day 5 and day 7 (P < 0.05) (Figure 2C). In the case of the DLD-1 tumors, the pharmacokinetics was similar to that of the NCI-H460 tumors with the highest T:M of 7.3 achieved at 3 days, but the ratios were ~2-fold lower compared to NCI-H460 tumors at all time points and consistent with lower TEM8 expression (Figure 2C). These data would suggest that the optimal imaging time was 3 days because it allowed sufficient time for clearance of [89]Zr-df−L2mAb from nontarget tissue while still retaining high activity in the target tissue.

Additional biodistribution studies with NCI-H460 xenografts were performed using [89]Zr-oxalate (which has a biodistribution characteristic of free Zr) to further distinguish specific [89]Zr-df−L2mAb binding to TEM8 in NCI-H460 tumors from the fraction of tumor uptake that may represent "free [89]Zr" resulting from [89]Zr-df−L2mAb metabolism.[32] Overall the free [89]Zr biodistribution was comparable to that reported in previously published studies in mice with the highest [89]Zr retention occurring in the bone at all time points of 1, 3, and 5 days which was at least 3- to 10-fold greater than all other tissues examined (figure not shown).[32,40] From these [89]Zr biodistributions the NCI-H460 T:M ratios of 3.20, 2.19, and 1.62 at 1, 3, and 5 days, respectively, were observed which steadily decreased over the time course failing to exhibit any specific tumor retention (Figure 2C). In contrast [89]Zr-df−L2mAb T:M ratios increased from 1 to 3 days exhibiting increased tumor retention which would be consistent with TEM8 specific binding. These studies would further indicate that the majority of the NCI-H460 T:M ratio represents [89]Zr-df−L2mAb binding with the free [89]Zr fraction ranging from 16% to 35% over the 5 day time course.

The total radioactive content of [89]Zr-df−L2mAb in NCI-H460 tumors (% ID per tumor) correlated to corresponding tumor weights which ranged from 0.26 to 3.46 g (R^2 = 0.92, $n = 9$) (figure not shown), but the significance of the correlation and slope (% ID/g) was affected by the distribution of the tumor weights. Tumors <2 g showed a highly significant correlation (R^2 = 0.99; slope = 5.2% ID/g; $n = 5$) while tumors >2 g had more variability with a less significant correlation and a lower slope indicating decreased uptake per g (% ID/g) of tumor (R^2 = 0.70, slope = 2.1% ID/g, $n = 4$). This is likely because the larger tumors exhibited regional necrosis where uptake per gram of tissue would be expected to be much lower.[40]

MicroPET Imaging Studies. MicroPET imaging studies with [89]Zr-df−L2mAb were performed in NCI-H460 and DLD-1 at 1, 3, and 5 days postinjection. Both NCI-H460 and DLD-1
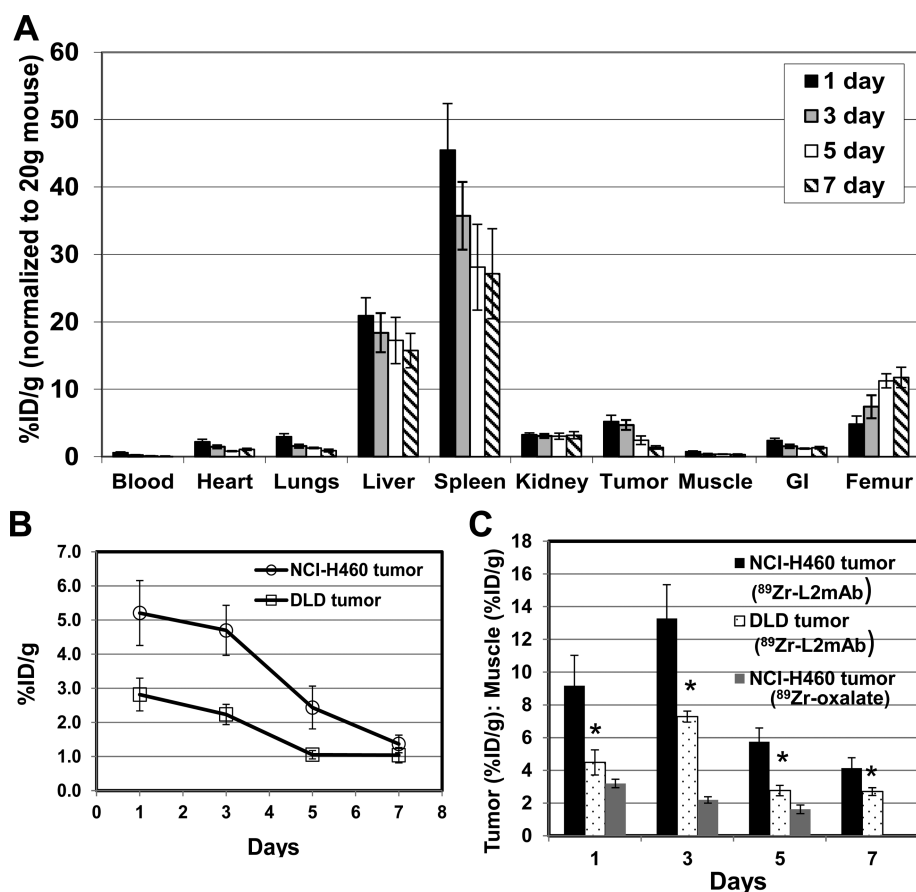
Figure 2. (A) Biodistribution of [89]Zr-df—L2mAb in NCI-H460 xenografts from 1 to 7 days. Each time point represents the mean % ID/g ± SD of [89]Zr-df—L2mAb ($n = 5$ each time point). (B) Comparison of [89]Zr-df—L2mAb uptakes (% ID/g) in DLD-1 and NCI-H460 tumors from 1 to 7 days. (C) Comparison of tumor (% ID/g):muscle (% ID/g) ratios (T:M) with (1) [89]Zr-df—L2mAb in NCI-H460 and DLD-1 xenografts from 1 to 7 days [bars represent mean T:M ± SD ($n = 5$); *significant increases between the NCI-H460 T:M ratios and DLD-1 T:M ratios at the same time points, $P < 0.05$]; (2) [89]Zr-oxalate in NCI-H460 xenografts from 1 to 5 days [bars represent mean T:M ± SD ($n = 3$)].

tumors were visualized as early as 1 day postinjection (Figure 3A,B). Although both NCI-H460 and DLD-1 tumors had sufficient radioactive uptake for imaging, lower [89]Zr-df—L2mAb uptakes were observed in the DLD-1 tumors and comparable to the biodistribution results. The [89]Zr-df—L2mAb retained in the NCI-H460 tumor remained relatively constant from day 1 to 3 as the tracer was washed out from nontarget organs. The NCI-H460 T:M ratios improved from 6:1 on day 1 to 12:1 at day 3 and decreased at day 5 to 3:1 comparable to the biodistribution results; DLD-1 T:M ratios were 1.5- to 2-fold lower than those of NCI-H460 at similar times and compared favorably also to biodistribution results.

In Vitro Autoradiography. In vitro autoradiography was performed to ascertain the specific regional localization of TEM8 in tumors from mouse xenografts; the cell lines used for the development of these tumors included NCI-H460 and DLD-1 with known in vitro high and low cellular TEM8 expression, respectively, as well as U87-MG, MKN-45, T-47D, and A-431 (Figure 4). For all the tumors [89]Zr-df—L2mAb specific binding was observed which was heterogeneous across the tumor sections resulting in high and low density binding regions which may reflect differences in TEM8 expression in the tumor vasculature and stroma compared to tumor cells. Further quantitative analysis was performed by drawing ROIs (PSL/mm^2) representing total or nonspecific [89]Zr-df—L2mAb binding (B_t or B_{nsb}) which encompassed either the whole section

or high and low density regions from which the specific regional TEM8 expression ($B_{sp} = B_t - B_{nsb}$) could be determined (Figure 5A). The high density ROIs from all the tumors and the whole section ROIs of U87-MG, T-47D, and NCI-H460 exhibited the highest specific [89]Zr-df—L2mAb binding ranging from 90% to 75% compared to the low density ROIs and whole section ROIs of A-431, DLD-1, and MKN-45 which had lower specific binding ranging from 70% to 30% (Figure 5A). The highest specific regional TEM8 concentrations in the high density ROIs (2700 to 480 PSL/mm^2) were 2- to 4-fold higher than those in the low density ROIs ($B_{sp} = 1260$ to 140 PSL/mm^2). U87-MG had the highest TEM8 concentrations for both the high (2694 PSL/mm^2) and low (1264 PSL/mm^2) density ROIs with ~2-fold differences between the high and low ROIs. On the other hand A431, DLD-1, and MKN-45 tumors had the lowest TEM8 concentrations for both the high (ranging from 562 to 480 PSL/mm^2) and low (ranging from 273 to 141 PSL/mm^2) density ROIs; nevertheless MKN-45 had a greater high to low density ROI ratio of ~4.

The relative molar concentrations (nM$_{rel}$) of TEM8 calculated from the tumor whole section ROIs (PSL/mm^2) were highest for U87-MG (72 nM$_{rel}$), T-47D (51 nM$_{rel}$), and NCI-H460 (30 nM$_{rel}$) with at least 2-fold lower concentrations in A-431, DLD-1, and MKN-45 (15 to 10 nM$_{rel}$); these whole section ROIs representing both tumor vasculature and tumor cells may serve as a better predictor of relative in vivo TEM8 concentrations. In addition, whole tumor sections were used for CD31 IHC staining
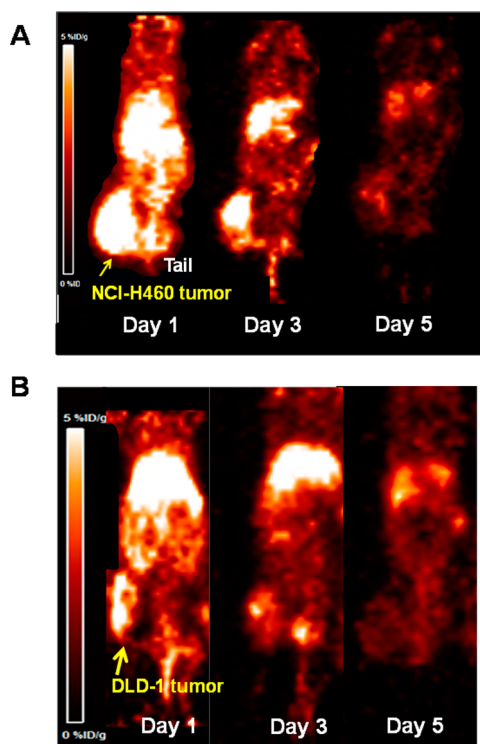
Figure 3. Representative coronal PET images of ^{89}Zr-df—L2mAb from a mouse with NCI-H460 (A) and DLD-1 (B) tumors on the right thigh at days 1, 3, and 5 after injection (iv).

and vessel density quantification; the vessel densities (vessels per 10^{-7} μm^2) from these sections of the 6 tumor types were comparable in rank order to the whole section ^{89}Zr-df—L2mAb specific binding (B_s, PSL/mm^2) with U87-MG tumors exhibiting the greatest vessel density (2214 vessels per 10^{-7} μm^2) and DLD-1, A-431, and MKN-45, 5- to 7-fold less (585 to 370 vessels per 10^{-7} μm^2) (Figure 5A). The vessel densities (vessels per 10^{-7} μm^2) of the 6 tumor types highly correlated to whole section ROIs (PSL/mm^2; $P = 0.0055$) indicating the association of increased TEM8 expression with increased tumor vascularization

(Figure 5B). The presence of the TEM8 protein in the 6 tumor types and cells was further confirmed by immunoprecipitation Western blotting (IP Western) in which TEM8 protein expression was detected in all 6 tumor types but not in DLD-1 or MKN-45 cells (Figure 5C). In particular high TEM8 expression was detected by IP Western and ^{89}Zr-df—L2mAb binding in both NCI-H460 cells and tumors, initially indicating that in vitro TEM8 concentrations of the tumor cells may be predictive of in vivo TEM8 concentrations in tumors. However, DLD-1 tumors exhibited much higher TEM8 levels than would have been predicted from in vitro DLD-1 cells which had undetectable or barely detectable TEM8 expression levels as determined by IP Western and ^{89}Zr-df—L2mAb binding, respectively.

■ DISCUSSION

Anti-TEM8 antibody (L2mAb) was successfully labeled with ^{89}Zr and exhibited high retention of its biological activity (immunoreactivity >82%) and high specific nanomolar binding affinity for the TEM8 receptor. High (HEK-293 F+), moderate (NCI-H460), and low/undetectable (DLD-1) TEM8 cell expression were quantitatively distinguished and comparable in rank order using both ^{125}I-L2mAb and ^{89}Zr-df—L2mAb which were consistent with TEM8 levels determined by IP Western and established TEM8 expression profiles for DLD-1.[24] In NCI-H460 and DLD-1 mouse xenografts the biodistribution and pharmacokinetics of ^{89}Zr-df—L2mAb in nontarget tissues were comparable with primarily hepatobiliary clearance typical for a large molecular weight protein such as the intact L2mAb (152 kDa). More importantly, ^{89}Zr-df—L2mAb was highly retained in NCI-H460 tumors, and the tumors were clearly discernible in PET images indicating high affinity TEM8 binding and TEM8 concentrations as predicted from in vitro studies with NCI-H460 cells. In similar in vivo studies ^{89}Zr-df—L2mAb retention in DLD-1 tumors was decreased ∼2-fold compared to NCI-H460 tumors but still visible in PET images. However, these higher DLD-1 tumor TEM8 concentrations were unexpected considering the low TEM8 expression in DLD-1 cells. Immunoprecipitation results confirmed that TEM8 levels were higher in DLD-1 tumors but undetectable in DLD-1 cells.
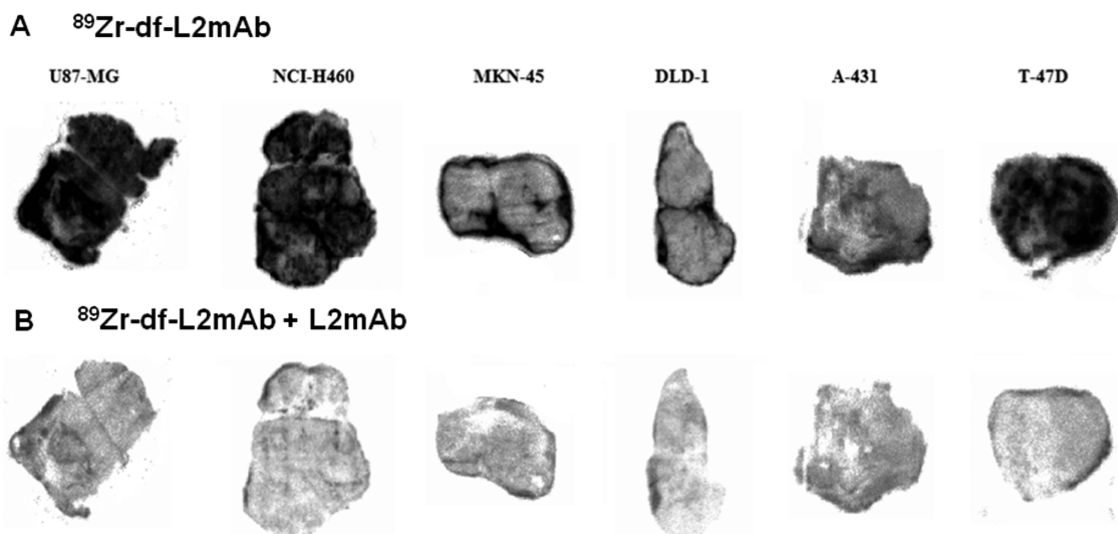
Figure 4. Autoradiograms of ^{89}Zr-df—L2mAb regional localization in tumor types U87-MG, NCI-H460, MKN-45, DLD-1, A-431, and T-47D (sections from near center of tumor): (A) total ^{89}Zr-L2mAb binding (B_t); (B) nonspecific ^{89}Zr-L2mAb binding [B_{nsb}: ^{89}Zr-df—L2mAb + L2mAb (10^{-6} M)].
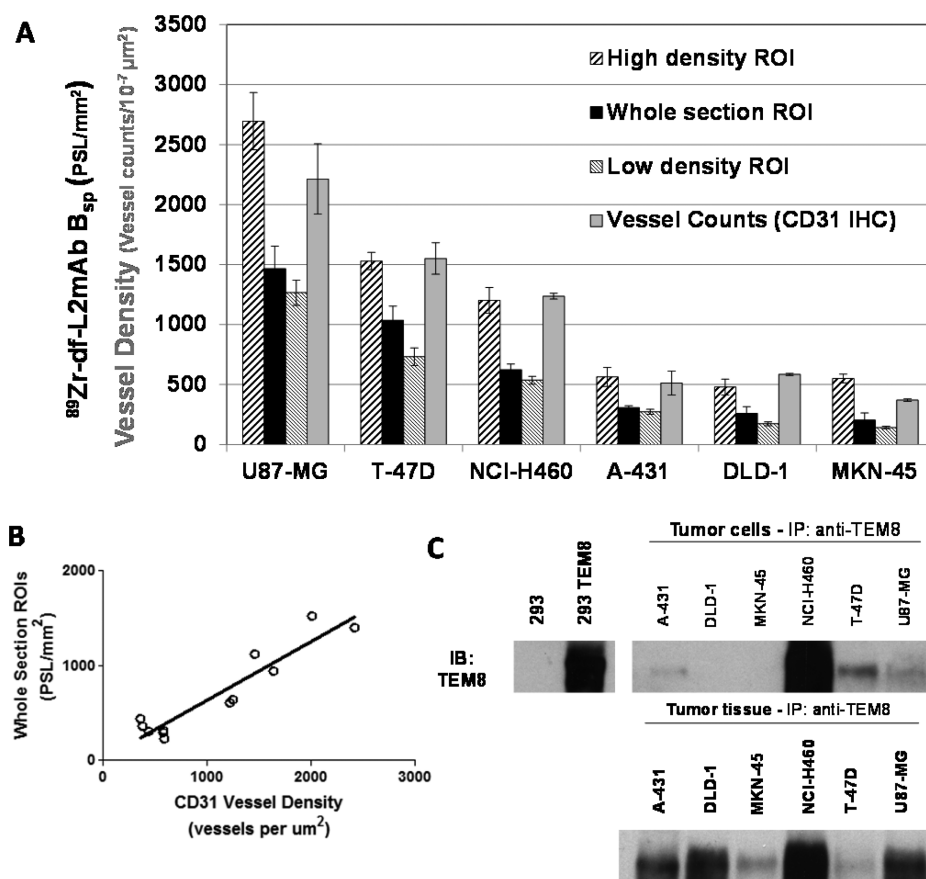
Figure 5. (A) Comparison of the quantitative regional distribution of ^{89}Zr-df–L2mAb in U87-MG, NCI-H460, T-47D, MKN-45, A-431,and DLD-1 tumor whole sections and specific ROIs of high and low density areas from in vitro autoradiography studies. Each bar represents the mean specific bound ^{89}Zr-df–L2mAb $\pm$ SD (B_{sp}; $B_t - B_{nsb}$) in photostimulated luminescence units per mm^2 (PSL/mm^2) calculated from ROIs representing total ^{89}Zr-L2mAb bound (B_t) and corresponding ROIs representing nonspecific binding ($+ 10^{-6}$ M L2mAb) [high density ROIs, $n = 4$; whole section ROIs, $n = 2$; low density ROIs, $n = 4$]. The bars representing quantitative vessel counts (vessel counts/10^{-7} μm^2) are the mean $\pm$ SD ($n = 2$) determined from CD31 IHC staining of whole sections. (B) Correlation of whole section ROIs (PSL/mm^2, ^{89}Zr-df–L2mAb specific binding) to vessel density (vessels per 10^{-7} μm^2), Spearman $r = 0.7622$, $P = 0.0055$. (C) Comparison of TEM8 protein in A431, DLD-1, MKN-45, NCI-H460, T-47D, and U87-MG cells and tumors determined by immunoprecipitation and Western blotting.

Since the DLD-1 and NCI-H460 tumors were of comparable mass (<2 g), these data would suggest that the increased DLD-1 tumor uptake is reflective of increased in vivo TEM8 expression, likely related to the presence of the tumor stroma.

From autoradiograms, ^{89}Zr-df–L2mAb binding was ∼2-fold higher for NCI-H460 tumors compared to DLD-1 tumors correlating with a 2-fold increase in vascularity determined from CD31 staining and vessel counts. Similarly ^{89}Zr-df–L2mAb binding in the high and low density regions of NCI-H460 tumors was 2- to 3-fold higher than that in the respective regions in DLD-1 tumors. These data indicate that the low density regions represent less tumor stroma and vasculature while the higher density regions would suggest a greater degree of vascularization. This 2- to 3-fold reduction of TEM8 concentrations in the whole DLD tumor sections (representative of a cross section obtained near the center point of the tumor), compared to NCI-H460 whole tumor sections, was comparable to the biodistribution results which might be expected since the in vivo ^{89}Zr-df–L2mAb tumor uptakes (% ID/g) represent an average of ^{89}Zr-df–L2mAb binding to both tumor cells and tumor vasculature. The IP Western results further confirmed the presence of TEM8 on both NCI-H460 cells and tumors, but for DLD-1 cells and tumors, TEM8 was detected only in tumors. Collectively these results would substantiate the hypothesis that TEM8

concentrations in DLD-1 tumors are related to the tissue stroma and not the tumor cell density. These results provide further confirmation to published findings in which immunofluorescent labeled L2mAb staining colocalized with CD31 staining in DLD-1 tumors indicating that TEM8 was associated with the tumor vasculature.[25] In vivo, DLD-1 tumors responded with decreased growth to treatment with L2mAb despite in vitro results demonstrating that L2 binding to DLD-1 cells was at background levels, providing further evidence that TEM8 is expressed in the host stroma and plays an important role in angiogenesis.[25]

Specific ^{89}Zr-df–L2mAb binding to TEM8 was found in every tumor type examined (NCI-H460, DLD-1, U87-MG, T-47D, MKN-45, and A-431) but varied ∼7-fold from the highest (U87-MG) to the lowest TEM8 expressors (MKN-45, DLD-1). These TEM8 expression levels highly correlated to vessel densities from CD31 staining indicating that the high density TEM8 regions would represent a greater degree of vasculature compared to low density TEM8 regions which would be composed of a greater degree of tumor cells. For the U87-MG tumors TEM8 expression levels varied ∼2-fold between the high and low density regions. These lower density regions most likely are a result of decreased tumor stroma in relation to tumor cells. Further, these findings of high TEM8 concentrations and vessel densities in

U87-MG tumors are consistent with the known vascular nature of U87-MG.[10,12] In contrast, the difference between the high (24 to 27 nM_{rel}) and low density regions of DLD-1 and MKN-45 tumors was much greater (~4-fold) compared to U87-MG high and low density regions; most likely this greater difference between the high and low density regions reflects regional increased DLD and MKN-45 tumor cell density which would be consistent with the undetectable TEM8 levels determined by IP Western. These results support immunohistochemical and gene/protein expression analysis that TEM8 is upregulated on tumor vessels whether or not the tumor cells express TEM8.[17,24,25] This would further suggest that tumors with intact stroma are required to determine relevant TEM8 densities as a prerequisite for predicting the suitability of TEM8 as an imageable target. With this in mind we would expect the relative TEM8 molar concentrations (nM_{rel}) of the whole tumor sections which ranged from 72 to 10 nM_{rel} to be the most reasonable approximation of in vivo TEM8 tumor concentrations. Using TEM8 nM_{rel} and the ^{89}Zr-df−L2mAb affinity constant ($K_d = 2$ nM) the potential in vivo target to nontarget ratios (T:NT) would be predicted to range from 36 to 5, which are derived from the mathematical model, B_{max}/K_d.[38,41] In particular these predicted T:NT ratios for NCI-H460 and DLD-1 of 15.4 and 6.5, respectively, compared favorably with the NCI-H460 and DLD-1 T:M ratios from the biodistribution studies of 9.2 to 13.3 and 4.5 to 7.3 from 1 to 3 days, respectively. Overall, these results would indicate that TEM8 is widely expressed across many different tumor types and for the most part in concentrations sufficient for imaging but uptake may not be predicted from in vitro expression. The high association of TEM8 expression with tumor stroma and vasculature further suggests that TEM8 targeted imaging agents could serve as a biomarker of tumor angiogenesis and in the selection of appropriate patients for anti-TEM8 therapy.

Although ^{89}Zr-df−L2mAb demonstrated adequate in vivo stability and targeting, further development may be required before clinical translation. The physical half-life of ^{89}Zr ($t_{1/2}$ ~ 3 d) is well matched to the biological half-life of L2mAb as optimal tumor to muscle ratios of 13:1 and 7:1 in NCI-H460 and DLD-1 tumors, respectively, were achieved at 3 days. Although the in vivo stability of ^{89}Zr-df−L2mAb was sufficient for PET imaging, the gradual uptake in bone suggests that some free ^{89}Zr is liberated from the conjugate due to metabolism.[40,42] The bone uptake does not interfere with the diagnostic accuracy of the conjugate, however, it may limit assessment of angiogenesis in the bone marrow as occurs in multiple myeloma and leukemia.[43−45]

This overall increased clearance and metabolism of ^{89}Zr-df−L2mAb although not typical for mAb targeting cell surface targets might be expected for mAb targeting vascular targets. Therapeutic mAbs have been found to have complex pharmacokinetics which are influenced by their target as well as their ability to elicit immune responses. For example cetuximab (human/murine chimeric IgG1) and panitumumab (human IgG2) have human plasma $t_{1/2}$'s of 3 and 7.5 days, respectively; although both target the same cell surface receptor (EGFR), only cetuximab has been reported capable of eliciting ADCC.[46] Therefore, L2mAb might be better compared to the anti-endoglin mAb, TRC105 (chimeric IgG1), which targets an endothelial receptor, CD105 (endoglin), that is overly expressed in proliferating tumor vasculature and induces ADCC.[47] The pharmacokinetics of TRC105 were dependent on dose. For instance, at the clinical trial dose (15 mg/kg) the serum $t_{1/2}$ was 1.78 days whereas at lower doses (3 and 10 mg/kg) the $t_{1/2}$'s were 0.31 day (7.4 h) and 0.45 day (10.8 h), respectively. This rate of clearance of TRC105 compares favorably to the blood $t_{1/2}$ of 1.5 days (exponential fit, $R^2 = 0.93$) found with ^{89}Zr-df−L2mAb. Further these complex pharmacokinetics may offer an explanation as to why in vivo specific ^{89}Zr-df−L2mAb binding cannot be proven with blocking studies using excess L2mAb. The enormous surface area of the vasculature is capable of acting as a "sink" for the TRC105 mAb which at lower concentration is subject to greater target antibody-mediated antibody clearance, whereas, at higher mAb concentrations, this targeted clearance is less efficient, therefore at smaller doses of mAb the serum clearance and $t_{1/2}$ would be faster.[46] These pharmacokinetics seem to be applicable to our ^{89}Zr-df−L2mAb biodistribution results in that an additional 500 μg of L2mAb coinjected with the ^{89}Zr-df−L2mAb dose (1 to 2 μg in mass) substantially increased (>40-fold) the ^{89}Zr-df−L2mAb blood radioactive content compared to the blood radioactivity content of the ^{89}Zr-df−L2mAb only low mass dose, indicating that this 500-fold increased L2mAb dose resulted in slower blood clearances with longer $t_{1/2}$'s. Although in vivo ^{89}Zr-df−L2mAb specific binding could not be proven with conventional blocking studies, the results from the ^{89}Zr-oxalate biodistribution studies would suggest specific targeting by ^{89}Zr-df−L2mAb as a 6-fold increase was observed in the ^{89}Zr-df−L2mAb NCI-H460 T:M ratios compared to the ^{89}Zr-oxalate NCI-H460 T:M ratios. Further ^{89}Zr-df−L2mAb was able to distinguish a 2-fold difference in TEM8 concentrations between NCI-H460 and DLD-1 tumors. These in vivo results coupled with the proven specific binding in vitro would indicate that ^{89}Zr-df−L2mAb is specifically targeting TEM8.

Improvement in the overall targeting of TEM8 and more rapid imaging might be accomplished by labeling an antibody fragment of L2mAb. L2mAb was designed as a targeted therapeutic molecule exerting potent antitumor activity by blocking TEM8 with an intact Fc capable of promoting antibody-dependent cellular cytotoxicity (ADCC) and complement dependent cytotoxicity (CDC).[25] These are desirable features in a therapeutic agent but may not be optimal for an imaging agent. So while an intact mAb may prove more therapeutically efficacious, antibody fragments with their faster clearance from nontarget tissue may be more suitable as radiolabeled imaging agents.[48,49]

In a variety of human tumor-bearing mouse models L2mAb treatment had potent antitumor activity with no detectable toxicities. In contrast current antiangiogenic targeted therapies have shown limited efficacy and greater associated toxicities resulting from interference with normal physiological processes (e.g., wound healing).[25] This apparent preferential expression of TEM8 in tumor vasculature would suggest that TEM8 is a potential target not only for further therapeutic development but for molecular imaging as well. TEM8 targeted PET imaging could aid in identifying angiogenic tumors that might be amenable to anti-TEM8 therapy. Moreover, PET imaging may aid in the drug development process by establishing appropriate dosing required for optimal tumor uptake, identifying nontarget tissues that may be associated with L2mAb toxicities and the associated tissue and organ pharmacokinetics of L2mAb in individual patients. Thus, ^{89}Zr-df−L2mAb represents a step forward in the PET imaging of tumor angiogenesis.

■ AUTHOR INFORMATION

Corresponding Author
*Molecular Imaging Program/NCI, 10 Center Dr. BLG10/RM B3B69, Bethesda, MD 20892-1088. Tel: 301-443-1661. Fax: 301-480-1434. E-mail: ejagoda@mail.nih.gov.

■ REFERENCES

(1) Seaman, S.; Stevens, J.; Yang, M. Y.; Logsdon, D.; Graff-Cherry, C.; St Croix, B. Genes that distinguish physiological and pathological angiogenesis. *Cancer Cell* **2007**, *11* (6), 539−54.

(2) Cryan, L. M.; Rogers, M. S. Targeting the anthrax receptors, TEM-8 and CMG-2, for anti-angiogenic therapy. *Front. Biosci.* **2011**, *16*, 1574−88.

(3) Kurdziel, K. A.; Lindenberg, L.; Choyke, P. L. Oncologic Angiogenesis Imaging in the clinic—how and why. *Imaging Med.* **2011**, *3* (4), 445−457.

(4) Niu, G.; Chen, X. PET Imaging of Angiogenesis. *PET Clin.* **2009**, *4* (1), 17−38.

(5) Collingridge, D. R.; Carroll, V. A.; Glaser, M.; Aboagye, E. O.; Osman, S.; Hutchinson, O. C.; Barthel, H.; Luthra, S. K.; Brady, F.; Bicknell, R.; Price, P.; Harris, A. L. The development of [(124)I]-iodinated-VG76e: a novel tracer for imaging vascular endothelial growth factor in vivo using positron emission tomography. *Cancer Res.* **2002**, *62* (20), 5912−9.

(6) Jayson, G. C.; Zweit, J.; Jackson, A.; Mulatero, C.; Julyan, P.; Ranson, M.; Broughton, L.; Wagstaff, J.; Hakannson, L.; Groenewegen, G.; Bailey, J.; Smith, N.; Hastings, D.; Lawrance, J.; Haroon, H.; Ward, T.; McGown, A. T.; Tang, M.; Levitt, D.; Marreaud, S.; Lehmann, F. F.; Herold, M.; Zwierzina, H. Molecular imaging and biological evaluation of HuMV833 anti-VEGF antibody: implications for trial design of antiangiogenic antibodies. *J. Natl. Cancer Inst.* **2002**, *94* (19), 1484−93.

(7) Nagengast, W. B.; de Korte, M. A.; Oude Munnink, T. H.; Timmer-Bosscha, H.; den Dunnen, W. F.; Hollema, H.; de Jong, J. R.; Jensen, M. R.; Quadt, C.; Garcia-Echeverria, C.; van Dongen, G. A.; Lub-de Hooge, M. N.; Schroder, C. P.; de Vries, E. G. 89Zr-bevacizumab PET of early antiangiogenic tumor response to treatment with HSP90 inhibitor NVP-AUY922. *J. Nucl. Med.* **2010**, *51* (5), 761−7.

(8) Cai, W.; Chen, K.; Mohamedali, K. A.; Cao, Q.; Gambhir, S. S.; Rosenblum, M. G.; Chen, X. PET of vascular endothelial growth factor receptor expression. *J. Nucl. Med.* **2006**, *47* (12), 2048−56.

(9) Kenny, L. M.; Coombes, R. C.; Oulie, I.; Contractor, K. B.; Miller, M.; Spinks, T. J.; McParland, B.; Cohen, P. S.; Hui, A. M.; Palmieri, C.; Osman, S.; Glaser, M.; Turton, D.; Al-Nahhas, A.; Aboagye, E. O. Phase I trial of the positron-emitting Arg-Gly-Asp (RGD) peptide radioligand 18F-AH111585 in breast cancer patients. *J. Nucl. Med.* **2008**, *49* (6), 879−86.

(10) Battle, M. R.; Goggi, J. L.; Allen, L.; Barnett, J.; Morrison, M. S. Monitoring tumor response to antiangiogenic sunitinib therapy with 18F-fluciclatide, an 18F-labeled alphaVbeta3-integrin and alphaV beta5-integrin imaging agent. *J. Nucl. Med.* **2011**, *52* (3), 424−30.

(11) Naumov, G. N.; Akslen, L. A.; Folkman, J. Role of angiogenesis in human tumor dormancy: animal models of the angiogenic switch. *Cell Cycle* **2006**, *5* (16), 1779−87.

(12) Zhang, X.; Xiong, Z.; Wu, Y.; Cai, W.; Tseng, J. R.; Gambhir, S. S.; Chen, X. Quantitative PET imaging of tumor integrin alphavbeta3 expression with 18F-FRGD2. *J. Nucl. Med.* **2006**, *47* (1), 113−21.

(13) auf dem Keller, U.; Bellac, C. L.; Li, Y.; Lou, Y.; Lange, P. F.; Ting, R.; Harwig, C.; Kappelhoff, R.; Dedhar, S.; Adam, M. J.; Ruth, T. J.; Benard, F.; Perrin, D. M.; Overall, C. M. Novel matrix metalloproteinase inhibitor [18F]marimastat-aryltrifluoroborate as a probe for in vivo positron emission tomography imaging in cancer. *Cancer Res.* **2010**, *70* (19), 7562−9.

(14) Whittaker, M.; Floyd, C. D.; Brown, P.; Gearing, A. J. Design and therapeutic application of matrix metalloproteinase inhibitors. *Chem. Rev.* **1999**, *99* (9), 2735−76.

(15) Chuang, C. H.; Chuang, K. H.; Wang, H. E.; Roffler, S. R.; Shiea, J. T.; Tzou, S. C.; Cheng, T. C.; Kao, C. H.; Wu, S. Y.; Tseng, W. L.; Cheng, C. M.; Hou, M. F.; Wang, J. M.; Cheng, T. L. In vivo positron emission tomography imaging of protease activity by generation of a hydrophobic product from a noninhibitory protease substrate. *Clin. Cancer Res.* **2012**, *18* (1), 238−47.

(16) St Croix, B.; Rago, C.; Velculescu, V.; Traverso, G.; Romans, K. E.; Montgomery, E.; Lal, A.; Riggins, G. J.; Lengauer, C.; Vogelstein, B.; Kinzler, K. W. Genes expressed in human tumor endothelium. *Science* **2000**, *289* (5482), 1197−202.

(17) Carson-Walter, E. B.; Watkins, D. N.; Nanda, A.; Vogelstein, B.; Kinzler, K. W.; St Croix, B. Cell surface tumor endothelial markers are conserved in mice and humans. *Cancer Res.* **2001**, *61* (18), 6649−55.

(18) Fernando, S.; Fletcher, B. S. Targeting tumor endothelial marker 8 in the tumor vasculature of colorectal carcinomas in mice. *Cancer Res.* **2009**, *69* (12), 5126−32.

(19) Nanda, A.; Carson-Walter, E. B.; Seaman, S.; Barber, T. D.; Stampfl, J.; Singh, S.; Vogelstein, B.; Kinzler, K. W.; St Croix, B. TEM8 interacts with the cleaved C5 domain of collagen alpha 3(VI). *Cancer Res.* **2004**, *64* (3), 817−20.

(20) Cullen, M.; Seaman, S.; Chaudhary, A.; Yang, M. Y.; Hilton, M. B.; Logsdon, D.; Haines, D. C.; Tessarollo, L.; St Croix, B. Host-derived tumor endothelial marker 8 promotes the growth of melanoma. *Cancer Res.* **2009**, *69* (15), 6021−6.

(21) Hotchkiss, K. A.; Basile, C. M.; Spring, S. C.; Bonuccelli, G.; Lisanti, M. P.; Terman, B. I. TEM8 expression stimulates endothelial cell adhesion and migration by regulating cell-matrix interactions on collagen. *Exp. Cell Res.* **2005**, *305* (1), 133−44.

(22) Bradley, K. A.; Mogridge, J.; Mourez, M.; Collier, R. J.; Young, J. A. Identification of the cellular receptor for anthrax toxin. *Nature* **2001**, *414* (6860), 225−9.

(23) Van der Vieren, M.; Crowe, D. T.; Hoekstra, D.; Vazeux, R.; Hoffman, P. A.; Grayson, M. H.; Bochner, B. S.; Gallatin, W. M.; Staunton, D. E. The leukocyte integrin alpha D beta 2 binds VCAM-1: evidence for a binding interface between I domain and VCAM-1. *J. Immunol.* **1999**, *163* (4), 1984−90.

(24) Chaudhary, A.; Hilton, M. B.; Seaman, S.; Haines, D. C.; Stevenson, S.; Lemotte, P. K.; Tschantz, W. R.; Zhang, X. M.; Saha, S.; Fleming, T.; St Croix, B. TEM8/ANTXR1 blockade inhibits pathological angiogenesis and potentiates tumoricidal responses against multiple cancer types. *Cancer Cell* **2012**, *21* (2), 212−26.

(25) Chaudhary, A.; St Croix, B. Selective blockade of tumor angiogenesis. *Cell Cycle* **2012**, *11* (12), 2253−9.

(26) Duan, H. F.; Hu, X. W.; Chen, J. L.; Gao, L. H.; Xi, Y. Y.; Lu, Y.; Li, J. F.; Zhao, S. R.; Xu, J. J.; Chen, H. P.; Chen, W.; Wu, C. T. Antitumor activities of TEM8-Fc: an engineered antibody-like molecule targeting tumor endothelial marker 8. *J. Natl. Cancer Inst.* **2007**, *99* (20), 1551−5.

(27) Felicetti, P.; Mennecozzi, M.; Barucca, A.; Montgomery, S.; Orlandi, F.; Manova, K.; Houghton, A. N.; Gregor, P. D.; Concetti, A.; Venanzi, F. M. Tumor endothelial marker 8 enhances tumor immunity in conjunction with immunization against differentiation Ag. *Cytotherapy* **2007**, *9* (1), 23−34.

(28) Ruan, Z.; Yang, Z.; Wang, Y.; Wang, H.; Chen, Y.; Shang, X.; Yang, C.; Guo, S.; Han, J.; Liang, H.; Wu, Y. DNA vaccine against tumor

endothelial marker 8 inhibits tumor angiogenesis and growth. *J. Immunother.* **2009**, *32* (5), 486–91.

(29) Yang, X.; Zhu, H.; Hu, Z. Dendritic cells transduced with TEM8 recombinant adenovirus prevents hepatocellular carcinoma angiogenesis and inhibits cells growth. *Vaccine* **2010**, *28* (43), 7130–5.

(30) Quan, Q.; Yang, M.; Gao, H.; Zhu, L.; Lin, X.; Guo, N.; Zhang, G.; Eden, H. S.; Niu, G.; Chen, X. Imaging tumor endothelial marker 8 using an 18F-labeled peptide. *Eur. J. Nucl. Med. Mol. Imaging* **2011**, *38* (10), 1806–15.

(31) McCabe, K. E.; Wu, A. M. Positive progress in immunoPET–not just a coincidence. *Cancer Biother. Radiopharm.* **2010**, *25* (3), 253–61.

(32) Abou, D. S.; Ku, T.; Smith-Jones, P. M. In vivo biodistribution and accumulation of 89Zr in mice. *Nucl. Med. Biol.* **2011**, *38*, 675–81.

(33) Perk, L. R.; Vosjan, M. J.; Visser, G. W.; Budde, M.; Jurek, P.; Kiefer, G. E.; van Dongen, G. A. p-Isothiocyanatobenzyl-desferrioxamine: a new bifunctional chelate for facile radiolabeling of monoclonal antibodies with zirconium-89 for immuno-PET imaging. *Eur. J. Nucl. Med. Mol. Imaging* **2009**, *37* (2), 250–9.

(34) Verel, I.; Visser, G. W.; Boellaard, R.; Stigter-van Walsum, M.; Snow, G. B.; van Dongen, G. A. 89Zr immuno-PET: comprehensive procedures for the production of 89Zr-labeled monoclonal antibodies. *J. Nucl. Med.* **2003**, *44* (8), 1271–81.

(35) Meares, C. F.; McCall, M. J.; Reardan, D. T.; Goodwin, D. A.; Diamanti, C. I.; McTigue, M. Conjugation of antibodies with bifunctional chelating agents: isothiocyanate and bromoacetamide reagents, methods of analysis, and subsequent addition of metal ions. *Anal. Biochem.* **1984**, *142* (1), 68–78.

(36) Vosjan, M. J.; Perk, L. R.; Visser, G. W.; Budde, M.; Jurek, P.; Kiefer, G. E.; van Dongen, G. A. Conjugation and radiolabeling of monoclonal antibodies with zirconium-89 for PET imaging using the bifunctional chelate p-isothiocyanatobenzyl-desferrioxamine. *Nat. Protoc.* **2010**, *5* (4), 739–43.

(37) Morris, B. J. Specific radioactivity of radioimmunoassay tracer determined by self-displacement: a re-evaluation. *Clin. Chim. Acta* **1976**, *73* (1), 213–6.

(38) Jagoda, E. M.; Vaquero, J. J.; Seidel, J.; Green, M. V.; Eckelman, W. C. Experiment assessment of mass effects in the rat: implications for small animal PET imaging. *Nucl. Med. Biol.* **2004**, *31* (6), 771–9.

(39) Seidel, J.; Vaquero, J. J.; Green, M. V. Resolution uniformity and sensitivity of the NIH ATLAS small animal PET scanner: comparison to simulated LSO scanners without depth-of-interaction capability. *IEEE Trans. Nucl. Sci.* **2003**, *50* (5), 1347–50.

(40) Jagoda, E. M.; Lang, L.; Bhadrasetty, V.; Histed, S.; Williams, M.; Kramer-Marek, G.; Mena, E.; Rosenblum, L.; Marik, J.; Tinianow, J. N.; Merchant, M.; Szajek, L.; Paik, C.; Cecchi, F.; Raffensperger, K.; Jose-Dizon, J. M.; Bottaro, D. P.; Choyke, P. Immuno-PET of the hepatocyte growth factor receptor Met using the 1-armed antibody onartuzumab. *J. Nucl. Med.* **2012**, *53* (10), 1592–600.

(41) Eckelman, W. C.; Mathis, C. A. Targeting proteins in vivo: in vitro guidelines. *Nucl. Med. Biol.* **2006**, *33* (2), 161–4.

(42) Nayak, T. K.; Garmestani, K.; Milenic, D. E.; Brechbiel, M. W. PET and MRI of metastatic peritoneal and pulmonary colorectal cancer in mice with human epidermal growth factor receptor 1-targeted 89Zr-labeled panitumumab. *J. Nucl. Med.* **2012**, *53* (1), 113–20.

(43) Borjesson, P. K.; Jauw, Y. W.; de Bree, R.; Roos, J. C.; Castelijns, J. A.; Leemans, C. R.; van Dongen, G. A.; Boellaard, R. Radiation dosimetry of 89Zr-labeled chimeric monoclonal antibody U36 as used for immuno-PET in head and neck cancer patients. *J. Nucl. Med.* **2009**, *50* (11), 1828–36.

(44) Hoeben, B. A.; Kaanders, J. H.; Franssen, G. M.; Troost, E. G.; Rijken, P. F.; Oosterwijk, E.; van Dongen, G. A.; Oyen, W. J.; Boerman, O. C.; Bussink, J. PET of hypoxia with 89Zr-labeled cG250-F(ab′)2 in head and neck tumors. *J. Nucl. Med.* **2010**, *51* (7), 1076–83.

(45) Dijkers, E. C.; Oude Munnink, T. H.; Kosterink, J. G.; Brouwers, A. H.; Jager, P. L.; de Jong, J. R.; van Dongen, G. A.; Schroder, C. P.; Lub-de Hooge, M. N.; de Vries, E. G. Biodistribution of 89Zr-trastuzumab and PET imaging of HER2-positive lesions in patients with metastatic breast cancer. *Clin. Pharmacol. Ther.* **2010**, *87* (5), 586–92.

(46) Dostalek, M.; Gardner, I.; Gurbaxani, B. M.; Rose, R. H.; Chetty, M. Pharmacokinetics, pharmacodynamics and physiologically-based pharmacokinetic modelling of monoclonal antibodies. *Clin. Pharmacokinet.* **2013**, *52* (2), 83–124.

(47) Rosen, L. S.; Hurwitz, H. I.; Wong, M. K.; Goldman, J.; Mendelson, D. S.; Figg, W. D.; Spencer, S.; Adams, B. J.; Alvarez, D.; Seon, B. K.; Theuer, C. P.; Leigh, B. R.; Gordon, M. S. A phase I first-in-human study of TRC105 (Anti-Endoglin Antibody) in patients with advanced cancer. *Clin. Cancer Res.* **2012**, *18* (17), 4820–9.

(48) Wu, A. M.; Olafsen, T. Antibodies for molecular imaging of cancer. *Cancer J.* **2008**, *14* (3), 191–7.

(49) Nayak, T. K.; Brechbiel, M. W. Radioimmunoimaging with longer-lived positron-emitting radionuclides: potentials and challenges. *Bioconjugate Chem.* **2009**, *20* (5), 825–41.